Research Article
Vol. 34, No. 10 / 18 May 2026 / *Optics Express* 17520

Optics EXPRESS

Dark-field synthetic-aperture digital holographic microscopy with an enhanced numerical aperture

MINWOO JUNG,[1] HOSUNG JEON,[1] SEONGJU LEE,[1] GUNHEE LEE,[1] YONGJUN LIM,[2,3,†] AND JOONKU HAHN[1,†,*]

[1] *School of Electronic and Electrical Engineering, Kyungpook National University, Republic of Korea*
[2] *Immersive Media Research Section, Media Research Division, Electronics and Telecommunications Research Institute, 218 Gajeong-ro, Yuseong-gu, Daejeon 34129, Republic of Korea*
[3] *yongjun@etri.re.kr*
[†] These authors contributed equally.
[*] *jhahn@knu.ac.kr*

Abstract: Synthetic-aperture digital holographic microscope (SA-DHM) has received attention in various fields due to its ability to achieve higher resolution images than single-shot optical microscopes. In SA-DHM, the numerical aperture (NA) is enhanced by capturing high spatial frequency information in the Fourier domain. This domain is divided into two regions based on the system NA: the bright-field region and the dark-field region. Specifically, the synthetic NA achievable with only bright-field measurements is limited to twice the system NA. Therefore, precise measurement of the dark-field region is essential for overcoming the limitations of conventional SA-DHMs. In most SA-DHMs, the illumination angle determines the position of the measured field in the Fourier domain, and the precise control of the illumination angle is important for high resolution. In this study, we developed a solid-state beam-steering optics using a digital micromirror device (DMD), avoiding the vibrations associated with mechanical steering optics such as galvano-mirrors. We also propose a calibration method to correct the k-vector for high-angle illumination. With our SA-DHM system, both bright-field and dark-field images are measured precisely, achieving high-resolution results with a synthetic NA that is 3.2 times larger than the system NA.

1. Introduction

The digital holographic microscope (DHM) has been actively researched as a significant metrology method and it has a potential to obtain the three-dimensional (3D) optical information of the object by measuring the interference between the reference wavefront and the object wavefront from the sample [1–3]. In DHMs, a system numerical aperture (NA) characterizes the range of angles over which the system can accept the optical information and it is typically equal to the NA of an objective lens. The space-bandwidth product (SBP) of the system is determined by the NA and the field of view (FOV), and there is a trade-off relationship between the NA and the FOV for a given SBP [4–8]. Therefore, it is one of the most challenging problems to realize a DHM with both high NA and wide FOV.

Synthetic-aperture (SA) technique is a popular method for obtaining high-resolution images and has been suggested as a solution to overcome the limitations of SBP in DHM [9–11]. In DHM, the SA method involves illuminating an object in multiple directions with beam-steering optics. The measured complex wave is converted by Fourier transform into the spatial frequency domain and its position is determined by the direction of the illumination. When the complex wave is synthesized, the NA of the resultant images is called a synthetic NA which is higher than the system NA [12]. The Fourier spectrum synthesized by the SA method is divided into bright field and dark field whether the illumination light is directly accepted by the system or

#592479
Journal © 2026
https://doi.org/10.1364/OE.592479
Received 3 Feb 2026; revised 28 Mar 2026; accepted 12 Apr 2026; published 4 May 2026

not. In the bright field, the illumination light is directly captured by the focal plane array (FPA) sensor. So, the spectrum of the bright field is intrinsically limited within twice the system NA [13,14–16]. On the other hand, when the angle of the illumination light is larger than the system NA of the DHM, the measured spectrum is called the dark field. In the dark field, the diffracted light with high spatial frequency over twice the system numerical aperture is measured [17–19]. In the dark-field image, high-frequency edges are prominent, whereas low spatial frequencies are suppressed in the bright field [20–23]. Therefore, in SA method, it is important to measure dark field for high resolution since the synthetic NA of the bright field is limited up to only twice the system NA.

In SA-DHMs, various beam-steering optical modules have been applied, which control the angle of illumination light. The most popular beam-steering optical module consists of galvano-mirrors and relay optics, where the galvano-mirrors rotate mechanically to change the direction of the incident light [24–26]. Then, the relay optics deliver the beam to the specimen. But galvano-mirrors have disadvantages which are sensitive to vibrations caused by mechanical movements, and the visibility of the interference pattern decreases. Furthermore, the low repeatability of galvano-mirrors leads to inaccuracies in measurement of the spectrum of object wave. Mico et al. also propose a SA-DHM system based on a two-dimensional point-source array and a corresponding pinhole array [27]. This method enables single-shot acquisition of multiple spatial-frequency components without active beam steering. However, because the finite pupil support is spatially partitioned by the pinhole array, the number of usable multiplexed frequency slots is limited, and dense high-angle dark-field acquisition is difficult. On the other hand, a digital micromirror device (DMD) is a solid-state modulation device [28,29] composed of micro-electromechanical systems (MEMS) mirrors. So, the DMD is intrinsically robust to vibration. In several cases, it has been used for steering the beam as a solid-state modulation device generating the binary pattern [30]. In these systems, the DMD generates linear gratings with variable period and diffracts the light in the designed direction. Additional $4f$ optics is used to filtering out the residue resulting from imperfect binarized discrete linear grating. Ref. [32] reports a DMD-based solid-state SA-DHM with a large SBP, but the use of a high-NA oil-immersion objective constrains deployment in general-purpose microscopy [31].

In this paper, a SA-DHM with solid-state beam-steering optics is proposed, which is capable to acquire both wide FOV and high NA. The proposed beam-steering optics comprises a DMD, $4f$ optics, a microlens array (MLA), and a condenser lens. A related DMD and MLA based angle-scanning module has also been reported by Yang et al., where the DMD is used as a spatial switch and the illumination angle is determined by the beam position at the MLA plane [32]. Although the optical configuration reported by Yang et al. is very similar to that used in this work, the optical design target is different. Their system is a non-interferometric ODT configuration in which the illumination and imaging NAs are nearly matched. In contrast, our SA-DHM is intentionally designed with an illumination NA much larger than the system NA in order to acquire high-angle dark-field data and extend the synthetic aperture beyond the bright-field limit. This method has practical benefits to control the illumination angle of the beam in wide range, since the DMD turn on the specific pixels for changing the position of the beam instead of diffracting the beam. Because the illumination angle of the beam depends on the transverse position at the MLA plane, there is no noise from the diffraction. In our previous research [33], we proved the feasibility of our method from the optical simulation results. In this paper, we implemented the SA-DHM with solid-state beam-steering optics and the synthetic NA is experimentally achieved 3.2 times larger than the system NA by measuring both bright field and dark field. For dark field measurement, the accuracy and reliability of the illumination angle by beam-steering optics are very important. So, a new calibration method is proposed where the linear grating is used as a specimen. Then, diffraction points are measured according to the change of the rotation angle of the linear grating. After the curve-fitting these points, the direction of the steered beam is obtained. With the proposed SA-DHM, wide-field high-resolution object images are successfully reconstructed.

2. Solid-state beam-steering optics for SA-DHM

In the proposed solid-state beam-steering optics, the direction of illumination is controlled by beam positioning rather than diffraction from the binary grating on the DMD. So, the inaccuracy of illumination angles caused by the imperfection of discrete binary gratings is reduced and it is possible to generate the illumination beam with high inclination angle. Figure 1 shows the schematic of the proposed SA-DHM system, where coherent 532-nm fiber-type laser is used as the light source. The light source is divided into a reference arm and an object arm via a fiber beam splitter. In the reference arm, the beam amplitude is tuned using a variable optical attenuator (VOA). Then, after a collimator and a beam splitter, it enters the sensor in a direction parallel to the optical axis. On the other hand, the beam of the object arm is modulated by the DMD with the attached TIR prism. Then, it enters the MLA after passing through the $4f$ optics. Because the MLA and condenser lens are in a $4f$ optical system relationship, the beam is also collimated on the sample plane. The object wave diffracted by the sample passes through the objective lens and the tube lens, then it is focused on the sensor. On the sensor plane, the object wave interferes with the reference wave, and a fringe pattern is obtained. The VOA is used to adjust the optical power of the reference wave in comparison with that of the object wave to obtain highly visible interference patterns within the dynamic range of the sensor.

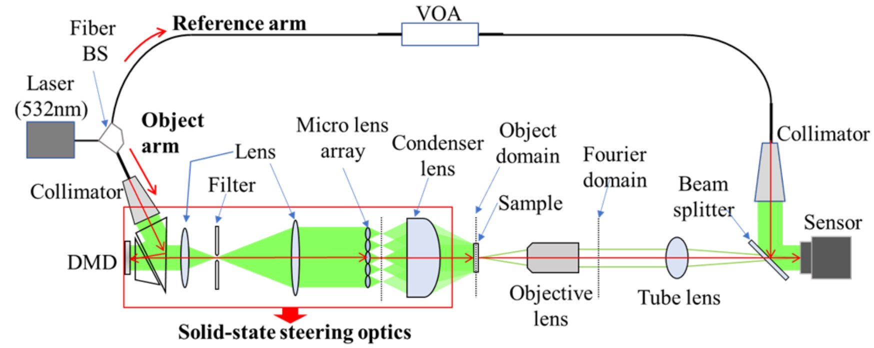

Fig. 1. Schematic of the proposed SA-DHM.

The beam-steering optical system comprises two $4f$ optics in series. The first $4f$ optical system delivers the wavefront from the DMD to the MLA. As shown in Fig. 2, the binary image on the DMD is a hexagonal array with circular apertures. Each aperture corresponds to an individual lens of MLA, where the beam modulated by the DMD is expressed as

$$U_{DMD,n}(u,v) = circ\left[\frac{(u-p_n)^2+(v-q_n)^2}{a^2}\right]. \tag{1}$$

Here, the output of circ function is one if the argument is less than or equal to one. Elsewhere, it becomes zero. So, the micromirrors of the DMD create a circular aperture with a radius, a, which is centered at $(p_n,\ q_n)$. n is the order of circular apertures assigned to each lens of the MLA. In the first $4f$ optical system, the higher-order diffraction components of the DMD are filtered out in the frequency domain. After the MLA, the beam is converged by the focal length

f_{MLA} of the lens of the MLA, and it is defined by

$$U_{MLA,n}(u',v') = U_{DMD,n}\left(\frac{u'}{M_1},\frac{v'}{M_1}\right)\exp\left[-j\frac{k}{2f_{MLA}}\{(u'-M_1p_n)^2+(v'-M_1q_n)^2\}\right], \tag{2}$$

where M_1 is the magnification of the first $4f$ optics and is equal to the focal length ratio f_2/f_1.

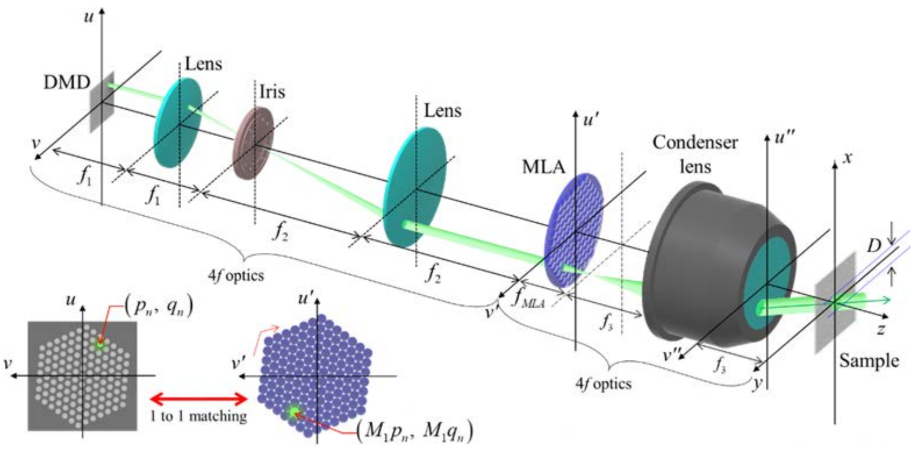

Fig. 2. Layout of the solid-state beam steering optics.

In the second $4f$ optics, the illumination angle increases as the center position of the beam $(p_n,\ q_n)$ on the DMD moves further away from the optical axis. This angle is specified by the k-vector, and its accuracy is important to place the spatial spectrum on the proper position of the Fourier domain. The n-th lens at positions $(M_1p_n,\ M_1q_n)$ of the MLA and the condenser lens are off-axis $4f$ optics. The beam passing through the n-th lens of the MLA propagates parallel to the optical axis until it reaches the condenser lens. After passing through the condenser lens, the beam becomes collimated and is directed toward the center of the back focal plane of the condenser lens.

Figure 3(a) shows how to estimate the k-vector of the illumination wave based on the design parameters of the optical system, where the illumination wave is represented as

$$U_{i,n}(x,y) = U_{DMD,n}\left(\frac{x}{M_1M_2}+p_n,\frac{y}{M_1M_2}+q_n\right)\exp[j(k_{i,n,x}x+k_{i,n,y}y)], \tag{3}$$

where M_2 is the focal length ratio f_3/f_{MLA} of the second $4f$ optics. f_3 is the effective focal length of the condenser lens and f_{MLA} is the focal length of the lens in MLA. The k-vector of the illumination beam from the n-th lens of the MLA is calculated using the following equation:

$$\overrightarrow{k}_{i,n} = \frac{k\sin\theta_{i,n}}{\sqrt{p_n^2+q_n^2}}(p_n\hat{x}+q_n\hat{y}). \tag{4}$$

Here, the illumination angle $\theta_{i,n}$ is determined by the position of the n-th lens of the MLA and the focal length of the condenser, and it is represented as

$$\theta_{i,n} = \tan^{-1}\left(\sqrt{(M_1p_n)^2+(M_1q_n)^2}/f_3\right). \tag{5}$$

The diameter of the illumination beam is calculated as

$$D = 2aM_1M_2 \tag{6}$$

Figure 3(b) shows the bright field-area composed of 19 circular apertures, where the red hexagon represents the border of system NA. Figure 3(c) shows dark-field area outside of the bright field, consisting of 108 circular apertures. In this paper, the total of 127 images with different spatial frequency components are obtained by sequentially turning on all circular apertures in the hexagonal array on the DMD. Details of the aperture selection near the bright-, dark-field boundary are provided in Supplement 1 Section 1.

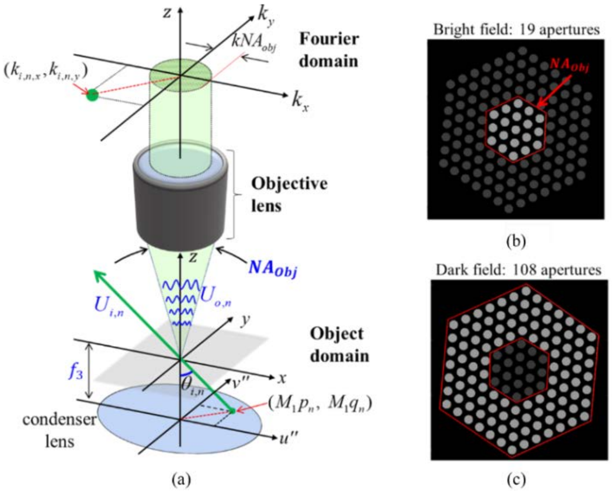

(a) (b) (c)

Fig. 3. (a) Relation between the object domain and the Fourier domain. (b) Regions corresponding to the bright field in DMD. (c) Regions corresponding to the dark field in DMD.

During the acquisition of the 127 spectra, the maximum illumination angle is denoted max $\theta_{i,n}$. The illumination NA s defined by

$$NA_i = \sin[\max(\theta_{i,n})] \tag{7}$$

And each single-shot measurement is bounded by the system numerical aperture NA_{sys}. In SA-DHM, the spectrum is shifted in the Fourier domain by the k-vector of illumination, so the synthetic NA extends by NA_i. The synthetic NA is therefore given by

$$NA_{syn} = NA_{sys} + NA_i \tag{8}$$

3. Calibration of solid-state beam steering optics

In SA-DHM, the accuracy and reliability of the illumination angle by beam-steering optics are very important. The error in the illumination angle deteriorates the quality of synthesized images. In our solid-state beam-steering optics, the error mainly comes from positional deviation of the MLA lens. So, we invented a calibration method by measuring the k-vector of illumination wave by the diffraction of a linear grating as shown in Fig. 4. Similar studies on illumination-angle or k-vector calibration have also been reported in Fourier ptychographic microscopy under bright-field and dark-field conditions [34–36]. In the present work, a rotating linear grating is used to calibrate the illumination k-vector in the interferometric SA-DHM system.

The illumination beam in a certain direction is diffracted by this linear grating sample, and higher-order diffractions are generated. These diffractions are described as

$$k_{dff,n,x} = \frac{2\pi m}{d} \cos\varphi + k \sin\theta_{i,n,x} \tag{9}$$

$$k_{diff,n,y} = \frac{2\pi m}{d} \sin\varphi + k \sin\theta_{i,n,y} \tag{10}$$

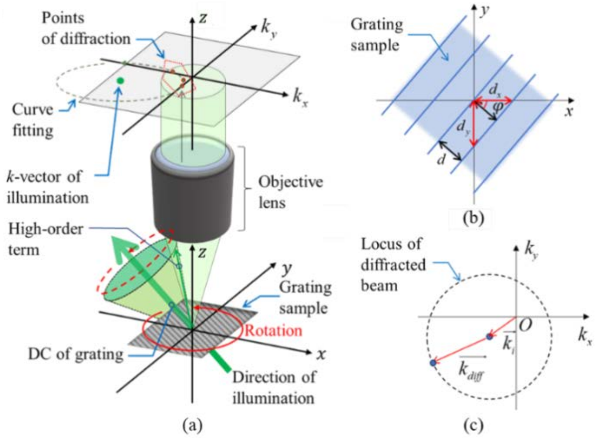

Fig. 4. (a) Setup for the measurement of the k-vector of the illumination beam according to the rotation of the linear grating. (b) Rotation geometry of the linear grating. (c) Locus of the diffracted illumination beam in the Fourier domain.

Here, d is the period of the linear grating and φ is the rotation angle around the center of the z-axis. m is the integer which represents the diffraction order.

The practical calibration procedure is illustrated in Fig. 5. Figure 5(a) shows calibration interferograms acquired by measuring the linear grating at different rotation angles. The Fourier transforms of these images are shown in Fig. 5(b), where the higher-order diffraction components of the linear grating are observed. Then, as shown in Fig. 5(c), representative positions are extracted in the Fourier domain from the selected higher-order diffraction components. For diffraction components corresponding to high-angle dark-field illumination, the representative position is defined as the local intensity maximum within the selected higher-order diffraction region. Finally, circle fitting is applied to the extracted positions to determine the center, which is used as the calibrated illumination k-vector. During calibration, the linear grating is mounted on a manual rotation stage and rotated about the z-axis over a 180° range. Because manual rotation is used, the angular intervals are not exactly uniform and are approximately 15°–22°. These circular trajectories have a common center point which is equal to the k-vector of the illumination wave. For each aperture, the illumination k-vector is determined from six or eight higher-order diffraction positions in the Fourier domain.

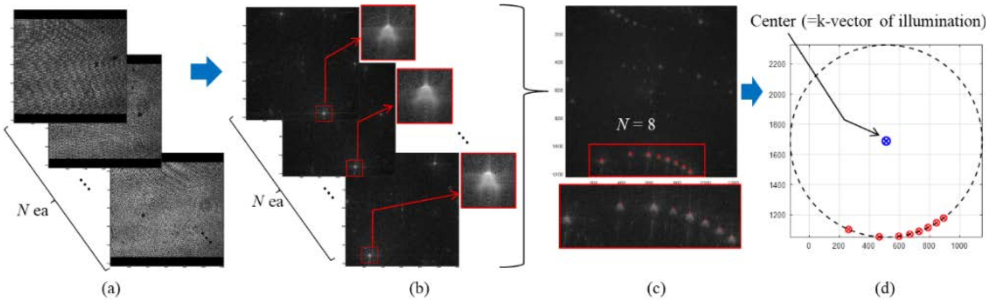

Fig. 5. Practical calibration procedure with linear grating. (a) Calibration images at multiple grating angles. (b) Fourier transforms of the calibration images. (c) Extracted higher-order diffraction positions. (d) Circle fitting for calibrated k-vector estimation.

In the present experiment, this calibration procedure is applied only to apertures on one side of shells 0 to 7 as shown in Fig. 6(a). The illumination k-vectors of the remaining apertures are then determined computationally by using the point-symmetry relation with respect to the Fourier-domain origin. This calibration method with a linear grating is practically useful because the illumination k-vector cannot be measured directly in the dark field. It can be estimated from the measurable higher-order diffraction components generated by a predetermined linear grating. Figure 6(a) shows seven representative apertures in different hexagonal shells, and Fig. 6(b) presents the extracted higher-order diffraction positions, the fitted circular trajectories, and the corresponding k-vector centers. Here, the red square indicates the frequency domain corresponding to the system NA, so only the grating diffraction components within this region are experimentally measurable. The red circular marks denote the first-order diffractions, the green circular marks denote the second-order diffractions, and the blue dots indicate the k-vector centers obtained by circle fitting.

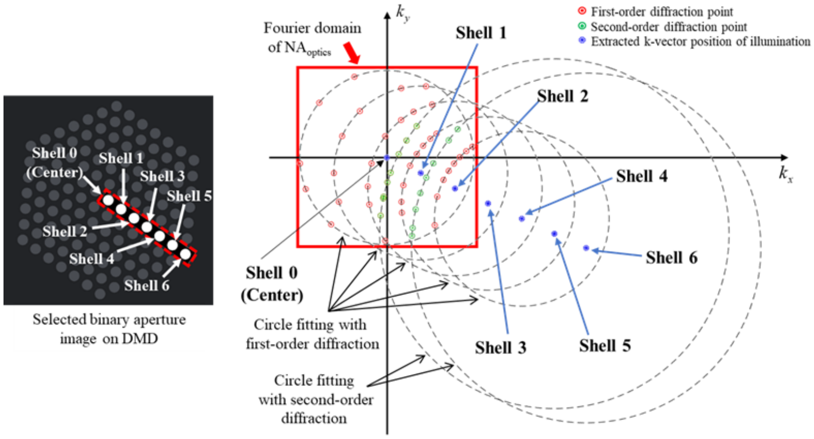

(a) (b)

Fig. 6. (a) Binary aperture array of the DMD used in the experiment. (b) Curve fitting results of the higher-order diffraction components of the linear grating in the Fourier domain.

Figure 7 compares the simulated and experimentally calibrated illumination angles. The black dots are the k-vector locations predicted in the Fourier domain by a Zemax simulation that assumes an ideal objective lens. The red points are the measured k-vector distribution obtained in our setup after rotating-grating calibration and thus reflect objective aberrations and small alignment offsets. The two distributions nearly coincide in the bright field but diverge toward the dark-field edge. The discrepancy grows as the paraxial approximation breaks down and aberrations, alignment errors, and medium mismatch accumulate. Accordingly, for the outermost k-vector in Fig. 7, the simulated illumination NA is approximately 0.41, whereas the experimentally calibrated value obtained by the rotating-grating method is approximately 0.40. Consequently, we regard the red distribution as the actual values. Based on this distribution, we set the illumination angles and carry out the SA reconstruction accordingly. A comparison of SA reconstructions obtained using the calculated and experimentally calibrated k-vector distributions is provided in Supplement 1 Section 2. Although some residual aberrations may still remain in the large-angle dark-field region, this reduces the propagation of large-angle errors into the reconstruction image.

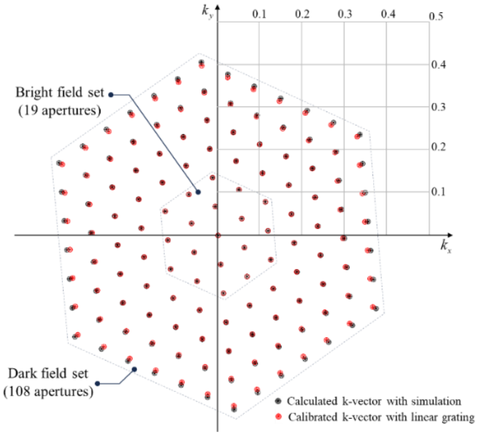

Fig. 7. Comparison of simulation and experimental calibration results of the illumination angles.

4. Synthesis of Fourier spectrum in SA-DHM

The synthesis algorithm for obtaining a large Fourier spectrum, including both bright field and dark field components, needs to be developed according to the system's characteristics. We will briefly introduce the structure of our SA-DHM system and the process of synthesizing the Fourier spectrum.

Figure 8(a) shows microscope part of the proposed SA-DHM system in detail. Since an infinity corrected objective is used, the object wave diffracted by the illumination light is focused with slightly diverging phase profile on the camera to record an image enlarged by the magnification of the objective lens. We use a pixelated polarization camera with a 2×2 micro-polarizer superpixel at analyzer angles 0°, 45°, 90°, and 135°. A quarter-wave plate (QWP) is placed immediately before the camera with its fast axis at 45°, which converts the two input linear states into opposite circular states. Each analyzer then projects both states with equal amplitude, so the four sub images provide phase steps of approximately 0°, 90°, 180°, and 270° in a single exposure. This single-shot acquisition avoids temporal phase scanning and reduces sensitivity to vibration and sample motion. The 45° QWP setting also balances the projections across the four analyzer channels, which improves the conditioning of the four-step reconstruction. Figure 8(b) shows the process of computing complex Fourier spectra of the object wave. In the first step, the four interference patterns with different phase shifts are acquired by the micro-polarization camera. The complex values of the object wave are calculated using the phase-shifting method [37,38]. Representative raw phase maps from selected individual aperture holograms and the corresponding phase maps after k-vector positioning are provided in Supplement 1 Section 3. In the last step, the signal is masked with a circular aperture whose size is equal to the system NA

Figure 9 shows the way to position the Fourier spectra of the n-th aperture. In Fig. 9, the red circle represents the Fourier spectrum of the on-axis illumination. The off-axis Fourier spectrum from the n-th aperture is shifted in the Fourier domain according to the calculated k-vector, $\vec{k}_{i,n}$. Each Fourier spectrum image is sequentially added, and high-frequency components are gradually filled via superposition with adjacent spectra. In this paper, the overlap ratio between two adjacent Fourier spectra is set to 80%. Figure 9(b) shows the total synthesized Fourier spectrum of the proposed SA-DHM system. Here, the resultant Fourier spectrum from both bright field and dark field is 3.2 times larger than the system NA.

To illustrate how the experimentally measured object waves are positioned and synthesized in the Fourier domain, representative bright-field and dark-field measurements are shown in

Optics EXPRESS

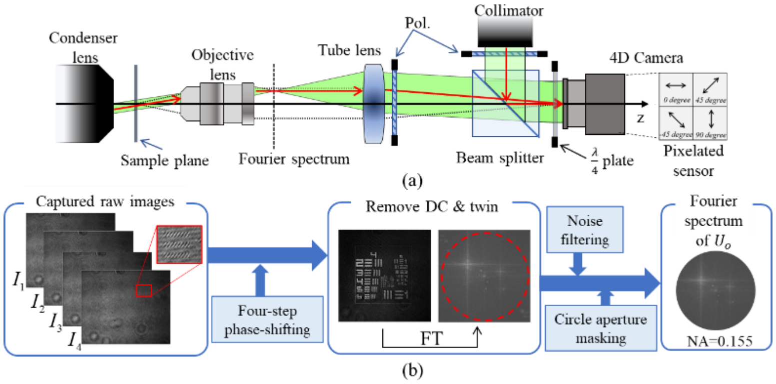

Fig. 8. (a) Microscope part of the proposed SA-DHM. (b) Process of computing complex Fourier spectrum from the captured image of micro-polarization camera.

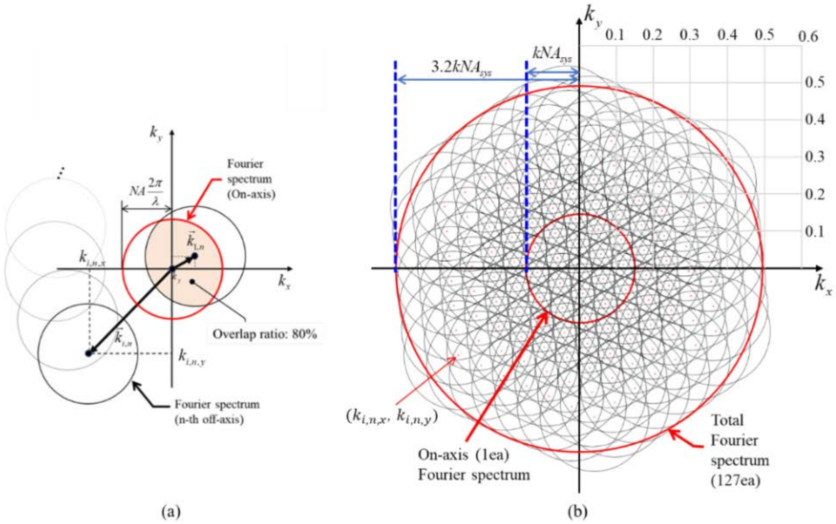

Fig. 9. (a) Positioning of the n-th off-axis Fourier spectrum and (b) total synthesized Fourier spectrum.

Figs. 10 and 11. As a specimen, a negative United State Air Force (USAF) target is used. The object waves from this specimen are measured by the micro-polarization camera. In our SA-DHM, 19 apertures are assigned to the bright-field region, and Figs. 10(a–c) show three representative binary apertures on the DMD. Figures 10(d–f) show the corresponding amplitude profiles, while Figs. 10(g–i) display the Fourier spectra of the same profiles. The USAF target consists of line pairs arranged in a rectangular shape, and the Fourier spectrum appears as a cross, with the intersection of this cross representing the k-vector of illumination. Since Figs. 10(g–i) correspond to the bright field, all the k-vectors of illumination are placed within a single-shot Fourier spectrum.

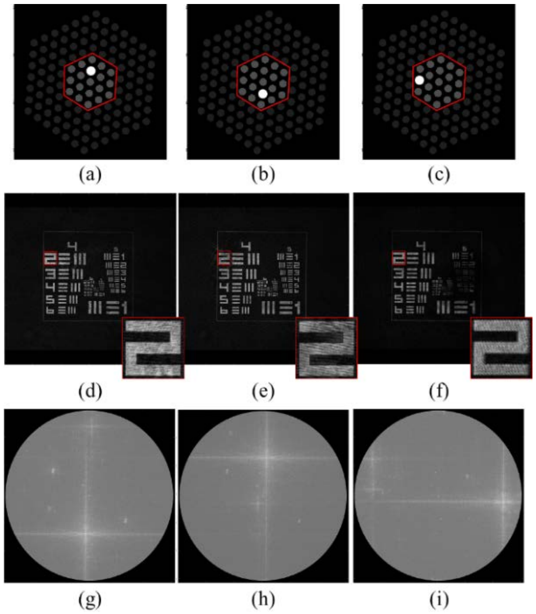

Fig. 10. Measurements of the object wave with respect to the directions of illumination. (a–c) Binary apertures in the bright field on the DMD. (d–f) Amplitude profiles and (g–i) Fourier spectra of the object wave corresponding to (a–c) under bright-field illumination, respectively.

Figure 11 shows the measurements in the dark field. In our SA-DHM, there are 108 apertures for the dark field and Figs. 11(a-c) show three of them. Figures 11(d-f) present dark-field amplitude profiles, where the object edges are most prominent. Tilting the illumination along x enhances vertical edges in Figs. 11(d) and 11(e), whereas tilting it along y enhances horizontal edges in Fig. 11(f). Figures 11(g–i) show the Fourier spectra corresponding to the amplitude profiles shown in Figs. 11(d–f), respectively. The k-vectors of the illumination are not observed since they are placed outside the single-shot Fourier spectrum. Instead, the high-frequency signals from the objects are captured, in contrast to those in the bright field. Therefore, as the illumination angle increases in the dark field, the resolution of the object image is naturally improved.

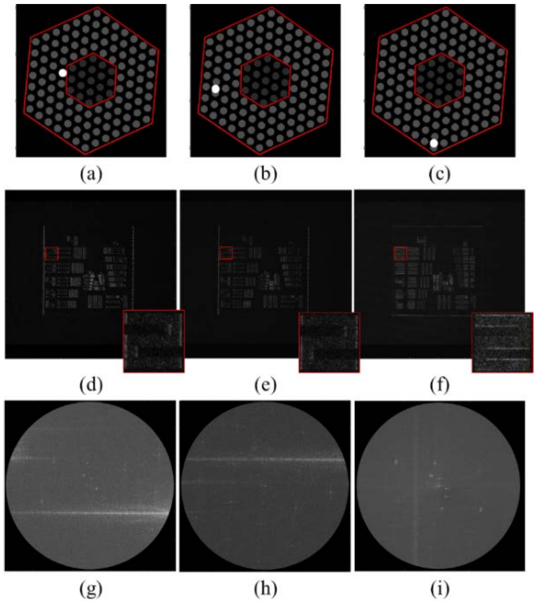

Fig. 11. Measurements of the object wave with respect to the directions of illumination. (a–c) Binary apertures in the dark field on the DMD. (d–f) Amplitude profiles and (g–i) Fourier spectra of the object wave corresponding to (a–c) under dark-field illumination, respectively.

5. Resolution enhancement by synthetic aperture

The entire optical system is composed of three main sections: the light source section, the illumination section, and the microscope section. The experimental setup of the proposed SA-DHM system is depicted in Fig. 12. The 532 nm, 200 mW laser output is delivered through a polarization-maintaining single-mode fiber (PM-SMF). A Thorlabs PN530R2F1 1 × 2 PM fiber coupler with a 10:90 split divides the power into the two arms. The reference arm receives ten percent of the power and the object arm receives ninety percent. Both arms are routed with Thorlabs P1-488PM-FC-2 PM patch cords to their respective fiber collimators. A V450 PA VOA is inserted in the reference arm before the collimator to balance the intensities. ADAFCPM2 PM mating sleeves with a narrow precision key are used for interconnections. All fibers are polarization-maintaining, and the PM slow axis is aligned with the laboratory horizontal so that the downstream polarizing optics and the polarization camera operate with stable input states. The illumination section contains solid-state beam-steering optics. The DMD has a resolution of 2,560 × 1,600 with a pixel pitch of 7.6 µm. The magnification of 4*f* optical system is 1.5, where an iris is inserted to remove undesirable high-order diffraction. The MLA has a total diameter of 25 mm, with an effective focal length of 3.26 mm and a lens pitch of 1.3 mm. The condenser lens has a NA of 0.78 and its working distance is 6.6 mm. In the microscope section, the objective lens manufactured by Navitar, Inc. has a magnification of 4 and a maximum NA of 0.2. The effective focal length of a standard tube lens is 200 mm. A 4D camera, BFS-U3-51S5P-C, with a CMOS-type FPA sensor has a resolution of 1,224 × 1,024 pixels. The native pixel pitch of the sensor is 3.45 µm, and the effective pixel pitch is 6.9 µm when the single-shot four-step phase-shifting scheme is considered. A quarter-wave plate QWP is placed in front of the 4D camera to measure the interference between the vertically polarized object wave and the horizontally polarized reference wave.

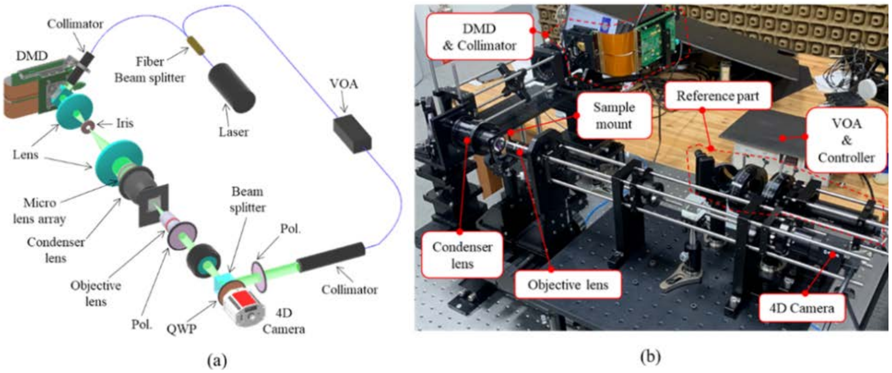

Fig. 12. Configuration of the proposed SA-DHM. (a) Schematic and (b) photo of the experimental setup.

Figure 13 shows synthesized results using our SA-DHM system with single-shot, only bright-field, and entire field. In Fig. 13(a), the system numerical aperture NA_{sys} with the single-shot aperture is 0.155, represented by the red circle in the circular Fourier spectrum. Using the effective pixel pitch of 6.9 µm, a wavelength of 532 nm, and the 4× microscope magnification, the sampling-limited NA is about 0.154, which is consistent with the observed Fourier-domain cutoff of about 0.155. This value is slightly smaller than NA of the objective lens, since most rectangular-shaped FPA sensors for the microscope are designed to be small size for fear of the vignetting effect. And NA_i that is numerical aperture of illumination is 0.41. In Fig. 13(b), the Fourier spectrum is synthesized by using 19 apertures which are bright fields. Here, the red circle is the maximum circle within the synthesized Fourier spectrum, whose NA is 0.262. In Fig. 13(c), all 127 apertures are synthesized, which possesses both bright-field and dark-field. The effective NA noted by the red circle reaches 0.495, which is approximately 3.2 times larger than the NA of a single shot. In Figs. 13(d–f), the reconstructed images are presented from Figs. 13(a-c), respectively. Regardless of the number of apertures, the FOV is 2.76 mm. Figures 13(g–i) show magnified images of Figs. 13(d–f) with groups 6 in the USAF target. In this scale, the contrast and sharpness of the patterns are well distinguishable for even single shot. However, the images are magnified once more in Figs. 13(j–l). In Fig. 13(j), the background noise is severe, and it is hard to distinguish the feature. In Fig. 13(k), the patterns in group 8 are significantly improved. In Fig. 13(l), the fine patterns in group 9 become clearly distinguishable.

Figure 14 shows the profiles of three example patterns in the reconstructed images of Figs. 13(d-f). For each case, the same mask size is applied to the selected USAF pattern in the reconstructed image, and the profile is obtained by averaging the pixel values along the y direction within the masked region. The black, blue, and red curves correspond to 1, 19, and 127 apertures, respectively, and the green curve is the ground truth. Figure 14(a) shows the change of the profiles for the pattern, element 2 in group 5 with a line width of 13.92 µm. Compared with the 19-aperture image (blue curve), the 127-aperture image (red curve) looks slightly noisier. This is because high-spatial-frequency speckles in the dark field is absent in the bright field. The modulation transfer function (MTF) increases with the number of apertures, as summarized in Table 1. The MTF is calculated from the contrast transfer function (CTF). Details are provided in the Appendix. Figure 14(b) shows the profiles for the pattern of group 7, element 6 (line width 2.19 µm). The period of the profiles is distinguishable for 1, 19, and 127 apertures. However, compared with Fig. 14(a), the profile edges are rounded because the higher spatial-frequency components of the periodic pattern are not transmitted through the apertures. The 127-aperture case still yields an MTF of 0.49 in Table 1. Figure 14(c) shows the profiles for the pattern of

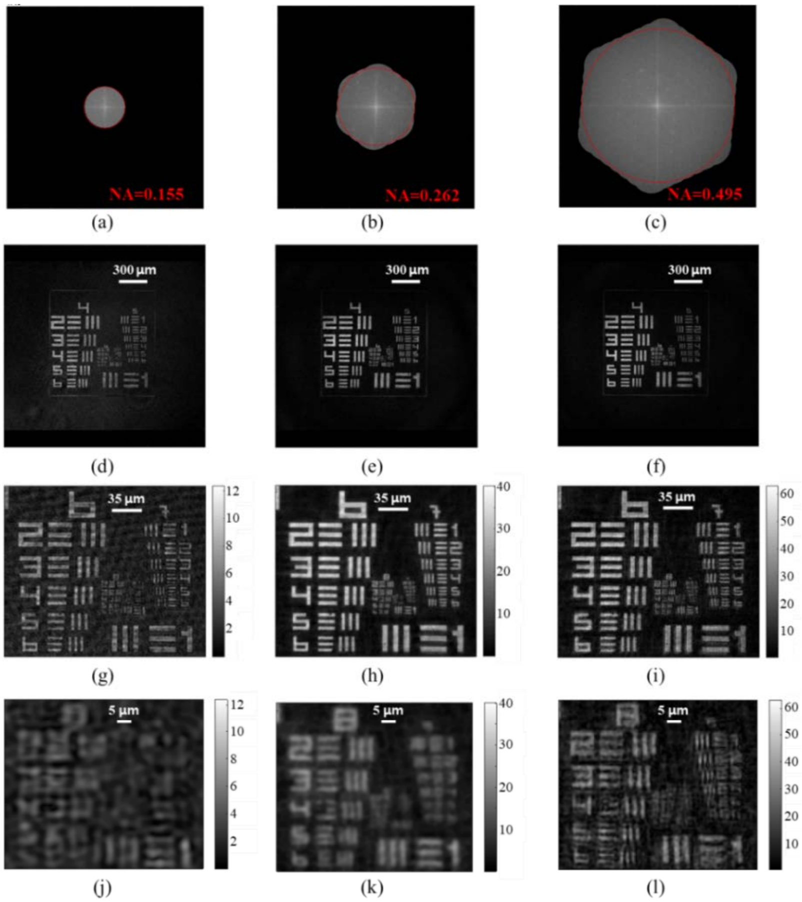

(a) (b) (c)

(d) (e) (f)

(g) (h) (i)

(j) (k) (l)

Fig. 13. Synthesized results with (a) 1, (b) 19, and (c) 127 apertures. (d–f) Amplitude profiles of the reconstructed object wave corresponding to (a–c). Enlarged reconstruction images from (g–i) group 6 and (j–l) group 8 corresponding to the expanded Fourier spectra in (a–c), respectively.

group 9, element 2 (line width 0.87 μm). In this case, only the 127-aperture profile exhibits the periodic pattern, because the spatial frequency corresponding to 0.87 μm is within the passband only for the 127 apertures synthesis. In Table 1, the MTF from 127 apertures is far superior to those from 1 and 19 apertures.

Table 1. MTF of USAF line widths of 13.92 μm, 2.19 μm, and 0.87 μm

Line width [μm]	Number of apertures		
	1	19	127
13.92	0.40	0.57	0.65
2.19	0.29	0.18	0.49
0.87	0.02	0.06	0.36

Figure 15 shows the MTFs with respect to the line width of USAF target from group 4 to group 9. The black and blue lines are MTFs from single and 19 apertures, respectively. The red line is MTF from 127 aperture of both bright field and dark field. The MTF from 19 apertures is

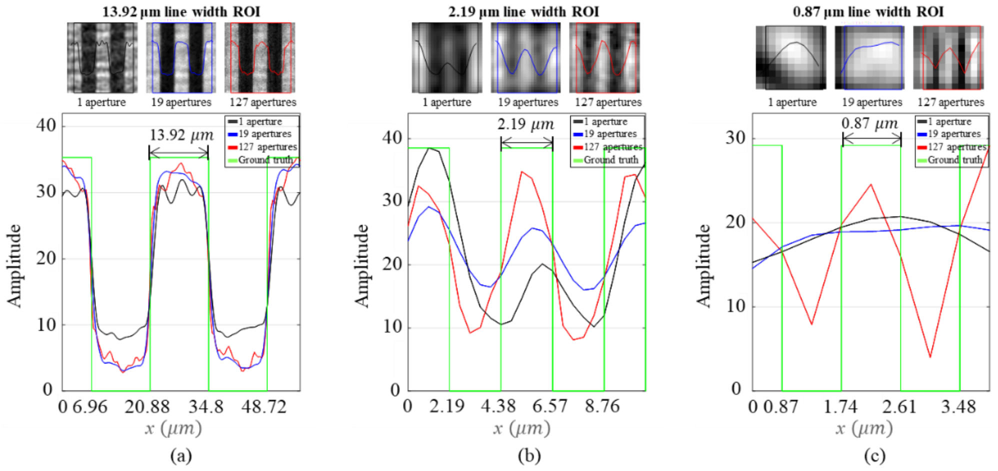

Fig. 14. Line profile comparison for reconstructed images obtained with 1, 19, and 127 apertures for binary patterns with line widths of (a) 13.92 µm (group 5, element 2), (b) 2.19 µm (group 7, element 6), and (c) 0.87 µm (group 9, element 2). Black: 1 aperture; Blue: 19 apertures; Red: 127 apertures; Green: ground truth.

slightly larger than that from a single aperture. This small difference should not be interpreted solely as the synthesis quality, because the present MTF is obtained from the CTF of a finite USAF rect pattern and may still be influenced by unexpected low-frequency components below the frequency of interest. In contrast, the MTF from 127 apertures is clearly larger than those from single and 19 apertures, which confirms the resolution enhancement by integrating both bright-field and dark-field spectra. The synthetic NA of our system is 0.495, which corresponds to a diffraction limit of 0.88 µm, since the light passing through the USAF target used in this experiment remains in-phase [39]. Our SA-DHM achieves excellent performance, achieving an MTF of 0.36 at 0.87 µm line width as shown in Fig. 14(c).

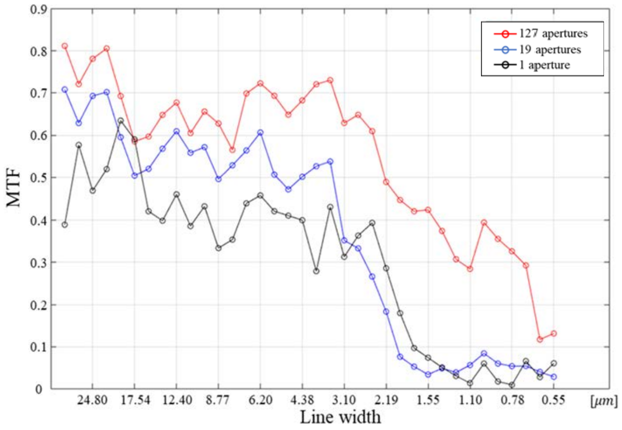

Fig. 15. MTFs from 1, 19, and 127 apertures with respect to the line width of USAF target from group 4 to group 9.

6. Discussion

In this paper, we propose a SA-DHM that integrates bright-field and dark-field information in the Fourier domain. This scheme extends the synthetic NA to more than twice that of the objective. Although the micro-polarization camera removes the need for temporal phase stepping within each aperture exposure, the full synthetic-aperture measurement still relies on 127 sequential acquisitions. In addition, the present work focuses on reliable high-angle dark-field acquisition by k-vector calibration using a rotating linear grating. To situate our approach relative to representative SA-DHM implementations, key specifications are summarized in Table 2. Most existing systems synthesize only bright-field data to improve resolution and typically employ objectives with a narrow FOV. For comparison, the SBP of Zheng et al.'s system is comparable to ours. They use an oil-immersion objective with a system NA of 1.3 and synthesize 39 bright-field spectra, achieving a synthetic NA of 2.29 over a 0.576 mm FOV. In our system, the system NA is 0.155 and 19 bright-field and 108 dark-field spectra are acquired to reach a synthetic NA of 0.495 over a 2.76 mm FOV. In the present wide-field configuration, this experimentally achieved NA is mainly limited by the usable illumination range required to maintain the 2.76 mm FOV and by the finite MLA diameter, rather than by the condenser NA alone. A schematic explanation of this illumination-NA limitation in the present wide-field configuration is provided in Supplement 1 Section 4. Refs. [25,26], and [31] also demonstrate their methods on cellular phase imaging and other practical samples, whereas this work focuses on system implementation, k-vector calibration, and resolution enhancement verified using a USAF target. Because the full SA measurement requires 127 sequential acquisitions, the present system is better suited to static or slowly varying samples than to rapidly changing live specimens. Based on the camera specification, the minimum camera-limited acquisition time for 127 sequential frames is approximately 1.7 s. The practical total acquisition time is longer because of additional overhead such as DMD pattern updating, data transfer, and reference-intensity adjustment. In addition, under dark-field conditions, the weak object signal requires balancing of the reference intensity to avoid saturation of the interference pattern, which we adjust using a VOA in our setup. However, increasing the number of apertures increases the acquisition time and introduces additional error sources in angle estimation, including sample misalignment, fluctuations in illumination power, speckle, and angle-calibration errors. Accordingly, single-exposure multiplexed SA approaches remain more suitable for fast dynamic imaging.

Table 2. Comparison of key specifications between representative SA-DHM systems reported in the literature and the proposed system (*Immersion objective lens)

	Our system	M. Kim [24]	Z. Huang [25]	C. Zheng [30]
Beam-steering device	DMD	Galvano scanner	Galvano scanner	DMD
Number of bright-field	19	36	4	39
Number of dark-field	108	0	0	0
Wavelength [nm]	532	632.8	632.8	532
FOV (Diameter) [mm]	2.76	0.2	0.59	0.576
$\mathbf{NA_{sys}}$	0.155	1.401*	0.419	1.3*
$\mathbf{NA_{syn}}$	0.495	2.2	0.7	2.29
Ratio of $\mathbf{NA_{syn}}$ to $\mathbf{NA_{sys}}$	3.2	1.57	1.67	1.76
Product of FOV and $\mathbf{NA_{syn}}$ [mm]	1.37	0.44	0.413	1.32
SBP($\times10^6$)	16.3	1.2	1.1	15.2

SBP is a dimensionless measure of spatial information capacity, equal to the number of optically resolvable elements within the FOV [40–42]. Because SBP scales inversely with the square of wavelength, the achromatic instruments such as microscopes show large SBP changes solely from wavelength selection, even when the underlying optical information capacity is unchanged. We therefore introduce a wavelength-independent figure of merit, the product of FOV and synthetic NA. For example, the systems in Refs. [25] and [26] operate at 632.8 nm. If the wavelength were changed to 532 nm, their SBP would increase by a factor of 1.41 without any optical modification. In contrast, the product of FOV and synthetic NA would remain unchanged.

7. Conclusion

In this study, we implemented a SA-DHM system with solid-state beam-steering optics to enhance illumination control and improve resolution. The proposed system utilizes a DMD, an MLA, and a condenser lens, where the DMD precisely adjusts the beam position without mechanical vibrations. To ensure accurate illumination angles, particularly for dark-field measurements, we introduced a calibration method using a linear diffraction grating. By analyzing the diffraction points at different rotation angles and applying curve-fitting in the Fourier domain, the actual k-vector position of the steered beam was estimated with high accuracy. Experimentally, by capturing and processing 127 bright-field and dark-field images, a wide-field, high-resolution object reconstruction was achieved. The synthetic NA of the system was experimentally verified to be 3.2 times larger than the original system NA, demonstrating a significant enhancement in the SBP. These results validate the effectiveness of the proposed SA-DHM system in achieving high-resolution imaging over an extended FOV. In the future, we aim to further enhance the quality of reconstructed images by directly compensating for the aperture-dependent aberrations associated with each MLA lens. Such correction is expected to improve the high-angle dark-field information and further enhance the ultimate resolution and image contrast of the reconstructed image.

Appendix: calculation details of the MTF

The MTF is a standard metric for quantifying image quality whose value varies with spatial frequency. It is typically evaluated at a specified frequency. The USAF target comprises three-bar rectangular elements rather than sinusoids, so the recorded pattern equals the object convolved with the system point-spread function. This convolution broadens the transitions, and the exterior edges (bar–background) exhibit different blur from the interior edges (between adjacent bars). Therefore, using the entire three-bar element introduces edge asymmetry and finite-window effects such as boundary discontinuities and the attendant frequency-domain broadening. To mitigate this, we define the region of interest to span exactly two central periods and exclude the outermost edges. This symmetric window preserves the dominant fundamental component while suppressing boundary artifacts, yielding a fair and reliable estimate of the CTF and the corresponding MTF at the specified spatial frequency.

In the region of interest, the CTF is evaluated along the horizontal x direction that is transverse to the bars. Let the region of interest r_{n_x,n_y} have size $(N_x,\ N_y)$. We first average the image samples along the y direction to form a one-dimensional profile,

$$\bar{r}_{n_x} = \frac{1}{N_y}\sum_{n_y=0}^{N_y-1} r_{n_x,n_y} \tag{11}$$

and then compute a one-dimensional DFT along x:

$$R_u = \sum_{n_x=0}^{N_x-1} \bar{r}_{n_x} e^{-j\frac{2\pi u}{N_x}n_x} \tag{12}$$

where $\mathrm{u} = 0, \cdots, N_x - 1$. Bin u corresponds to the object-space spatial frequency

$$f_x = \frac{u}{N_x M p} \tag{13}$$

with M the microscope magnification and p the camera pixel pitch. The CTF at f_x is obtained by normalizing the harmonic by the DC component,

$$CTF\left(f_x = \frac{u}{N_x Mp}\right) = 2\left|\frac{R_u}{R_{u=0}}\right| \tag{14}$$

As noted above, each region of interest spans exactly two periods of the bar pattern. Consequently, the dominant harmonic appears at $u = 2$ and the next nonzero harmonic appears at $u = 6$. That is because an ideal 50%-duty rectangular pattern exhibits odd symmetry which suppresses even harmonics. Using the standard bar-to-sine conversion, the MTF at this test frequency is given by

$$MTF = \frac{\pi}{4} CTF\left(f_x = \frac{2}{N_x Mp}\right) \tag{15}$$

The Eq. (15) is valid when the cut-off frequency is set to remain only the first term [43]. For each element, we choose the two-period window so that the frequency $f_x = 2/(N_x Mp)$ is dominant. If we consider the dominant term only, it means that the cut-off frequency is set to be between the dominant term and third harmonics. So, high-order harmonics are rejected by the optical transfer and the only dominant term is left. In most imaging systems only intensity is recorded, not the complex field. Because the phase is lost, an exact inverse mapping is not guaranteed, and Fourier-domain filtering is generally non-invertible. The spatial-frequency spectrum of the image is bounded by the system NA, but the exact boundary of the optical stop cannot be recovered from the image alone. By contrast, digital holography reconstructs the complex field, allowing the spatial-frequency spectrum to be further constrained by frequency-domain filters in digital signal processing.

Funding. Ministry of Culture, Sports and Tourism (RS-2024-00442410).

Acknowledgment. This research was supported by Culture, Sports and Tourism R&D Program through the Korea Creative Content Agency grant funded by the Ministry of Culture, Sports and Tourism in 2024 (Project Name: Development of optical technology and sharing platform technology to acquire digital cultural heritage for high quality restoration of composite materials cultural heritage, Project Number: RS-2024-00442410, Contribution Rate: 100%).

Disclosures. The authors declare no conflicts of interest.

Data availability. Data underlying the results presented in this paper are not publicly available at this time but may be obtained from the authors upon reasonable request.

Supplemental document. See Supplement 1 for supporting content.

References

1. M. K. Kim, "Principles and techniques of digital holographic microscopy," SPIE Rev. **1**, 018005 (2010).
2. M. K. Kim, *Digital Holographic Microscopy* (Springer, 2011).
3. E. Cuche, P. Marquet, and C. Depeursinge, "Spatial filtering for zero-order and twin-image elimination in digital off-axis holography," Appl. Opt. **39**(23), 4070–4075 (2000).
4. M. Rubin, G. Dardikman, S. K. Mirsky, *et al.*, "Six-pack off-axis holography," Opt. Lett. **42**(22), 4611–4614 (2017).
5. G. Dwivedi, L. Pensia, V. Lohchab, *et al.*, "Non-destructive inspection and quantification of soldering defects in PCB using an autofocusing digital holographic camera," IEEE Trans. Instrum. Meas. **72**, 1–8 (2023).
6. A. Anand, V. K. Chhaniwal, and B. Javidi, "Imaging embryonic stem cell dynamics using quantitative 3D digital holographic microscopy," IEEE Photonics J. **3**(3), 546–554 (2011).
7. W. Moon, H. Jeon, S. Park, *et al.*, "Seamless holographic image generation for a multi-vision system," J. Inf. Disp. **23**(4), 287–298 (2022).
8. M. Schürmann, Jana Scholze, Paul Müller, *et al.*, "Refractive index measurements of single, spherical cells using digital holographic microscopy," in *Methods in Cell Biology*, Vol. 125 (Elsevier, 2015), pp. 143–159.
9. Y. C. Lin, H. Y. Tu, X. R. Wu, *et al.*, "One-shot synthetic aperture digital holographic microscopy with non-coplanar angular-multiplexing and coherence gating," Opt. Express **26**(10), 12620–12631 (2018).
10. J. M. Rodenburg, "Ptychography and related diffractive imaging methods," Adv. Imaging Electron Phys. **150**, 87–184 (2008).
11. P. C. Konda, L. Loetgering, K. C. Zhou, *et al.*, "Fourier ptychography: current applications and future promises," Opt. Express **28**(7), 9603–9630 (2020).

12. P. Gao and C. Yuan, "Resolution enhancement of digital holographic microscopy via synthetic aperture: a review," Light Adv. Manuf. **3**(1), 105–120 (2022).
13. M. Liang and C. Yang, "Implementation of free-space Fourier ptychography with near maximum system numerical aperture," Opt. Express **30**(12), 20321–20332 (2022).
14. X. J. Lai, H. Y. Tu, C. H. Wu, *et al.*, "Resolution enhancement of spectrum normalization in synthetic aperture digital holographic microscopy," Appl. Opt. **54**(1), A51–A58 (2015).
15. K. Guo, S. Dong, G. Zheng, *et al.*, "Fourier ptychography for brightfield, phase, darkfield, reflective, multi-slice, and fluorescence imaging," IEEE J. Sel. Top. Quantum Electron. **22**(4), 77–88 (2016).
16. J. Zhang, T. Xu, S. Chen, *et al.*, "Efficient colorful Fourier ptychographic microscopy reconstruction with wavelet fusion," IEEE Access **6**, 31729–31739 (2018).
17. K. F. Tamrin, B. Rahmatullah, and S. M. Samuri, "An experimental investigation of three-dimensional particle aggregation using digital holographic microscopy," Opt. Laser Eng. **68**, 93–103 (2015).
18. J. L. Di, Y. Li, K. Q. Wang, *et al.*, "Quantitative and dynamic phase imaging of biological cells by digital holographic microscopy using a beam displacer unit," IEEE Photonics J. **10**(4), 1–10 (2018).
19. V. R. Besaga, A. V. Saetchnikov, N. C. Gerhardt, *et al.*, "Digital holographic microscopy for sub-μm scale high aspect ratio structures in transparent materials," Opt. Laser Eng. **121**, 441–447 (2019).
20. P. F. Gao, G. Lei, and C. Z. Huang, "Dark-field microscopy: recent advances in accurate analysis and emerging applications," Anal. Chem. **93**(11), 4707–4726 (2021).
21. T. Denneulin, F. Houdellier, and M. Hÿtch, "Differential phase-contrast darkfield electron holography for strain mapping," Ultramicroscopy **160**, 98–109 (2016).
22. T. van Gardingen-Cromwijk, S. Konijnenberg, W. Coene, *et al.*, "Non-isoplanatic lens aberration correction in dark-field digital holographic microscopy for semiconductor metrology," Light Adv. Manuf. **4**(4), 1–465 (2023).
23. L. Nigamatzyanova and R. Fakhrullin, "Dark-field hyperspectral microscopy for label-free microplastics and nanoplastics detection and identification in vivo: A *Caenorhabditis elegans* study," Environ. Pollut. **271**, 116337 (2021).
24. M. Kim, Y. Choi, C. Fang-Yen, *et al.*, "High-speed synthetic aperture microscopy for live cell imaging," Opt. Lett. **36**(2), 148–150 (2011).
25. Z. Huang, F. Yang, B. Liu, *et al.*, "Aberration-free synthetic aperture phase microscopy based on alternating direction method," Opt. Laser Eng. **160**, 107301 (2023).
26. C. J. Cheng, X. J. Lai, and Y. C. Lin, "Superresolution imaging in synthetic aperture digital holographic microscopy," in *Proc. IEEE Int. Conf. Photonics (ICP)* (IEEE, 2013), pp. 215–217.
27. J. Fan, X. Tang, X. Bi, *et al.*, "High-fidelity reconstruction of structured illumination microscopy by an amplitude-phase channel attention network with multitemporal information," IEEE Trans. Instrum. Meas. **72**, 1–13 (2023).
28. V. Mico, Z. Zalevsky, P. García-Martínez, *et al.*, "Synthetic aperture superresolution with multiple off-axis holograms," J. Opt. Soc. Am. A **23**(12), 3162–3170 (2006).
29. C. Fan, H. Zhao, Z. Zhao, *et al.*, "High-accurate quantitative phase imaging based on the transport of intensity equation and wavelet transform," IEEE Trans. Instrum. Meas. **72**, 1–11 (2023).
30. S. Shin, K. Kim, J. Yoon, *et al.*, "Active illumination using a digital micromirror device for quantitative phase imaging," Opt. Lett. **40**(22), 5407–5410 (2015).
31. C. Zheng, D. Jin, Y. He, *et al.*, "High spatial and temporal resolution synthetic aperture phase microscopy," Adv. Photonics **2**(06), 065002 (2020).
32. S. Yang, J. Kim, M. E. Swartz, *et al.*, "DMD and microlens array as a switchable module for illumination angle scanning in optical diffraction tomography," Biomed. Opt. Express **15**(10), 5932–5946 (2024).
33. H. Jeon, M. Jung, G. Lee, *et al.*, "Aberration estimation for synthetic aperture digital holographic microscope using deep neural network," Sensors **23**(22), 9278 (2023).
34. R. Eckert, Z. F. Phillips, and L. Waller, "Efficient illumination angle self-calibration in fourier ptychography," Appl. Opt. **57**(19), 5434–5442 (2018).
35. C. Zheng, S. Zhang, D. Yang, *et al.*, "Robust full-pose-parameter estimation for the led array in fourier ptychographic microscopy," Biomed. Opt. Express **13**(8), 4468–4482 (2022).
36. R. You and R. Liang, "Self-calibrating fourier ptychographic microscopy using automatic differentiation," Opt. Lett. **50**(2), 415 (2025).
37. X. Wang, D. Zhu, W. Shi, *et al.*, "Multi-depth-of-field 3-D profilometry for a microscopic system with telecentric lens," IEEE Trans. Instrum. Meas. **71**, 1–9 (2022).
38. T. Tahara, R. Yonesaka, S. Yamamoto, *et al.*, "High-speed three-dimensional microscope for dynamically moving biological objects based on parallel phase-shifting digital holographic microscopy," IEEE J. Sel. Top. Quantum Electron. **18**(4), 1387–1393 (2012).
39. N. Nill, "Conversion between sine wave and square wave spatial frequency response of an imaging system" (MITRE Corporation, 2001), pp. 1–44.
40. Y. Cotte, F. Toy, P. Jourdain, *et al.*, "Marker-free phase nanoscopy," Nat. Photonics **7**(2), 113–117 (2013).
41. J. Park, D. J. Brady, G. Zheng, *et al.*, "Review of bio-optical imaging systems with a high space-bandwidth product," Adv. Photonics **3**(04), 044001 (2021).
42. H. Wang, Z. Göröcs, W. Luo, *et al.*, "Computational out-of-focus imaging increases the space–bandwidth product in lens-based coherent microscopy," Optica **3**(12), 1422–1429 (2016).

43. J. W. Goodman, *Introduction to Fourier Optics*, 3rd ed. (Roberts & Company, 2005).